NANOMATERIALS

Robust epitaxial growth of two-dimensional heterostructures, multiheterostructures, and superlattices

Zhengwei Zhang,[1]* Peng Chen,[1,3]* Xidong Duan,[1]† Ketao Zang,[2] Jun Luo,[2] Xiangfeng Duan[1,3]†

We report a general synthetic strategy for highly robust growth of diverse lateral heterostructures, multiheterostructures, and superlattices from two-dimensional (2D) atomic crystals. A reverse flow during the temperature-swing stage in the sequential vapor deposition growth process allowed us to cool the existing 2D crystals to prevent undesired thermal degradation and uncontrolled homogeneous nucleation, thus enabling highly robust block-by-block epitaxial growth. Raman and photoluminescence mapping studies showed that a wide range of 2D heterostructures (such as WS_2-WSe_2 and WS_2-$MoSe_2$), multiheterostructures (such as WS_2-WSe_2-MoS_2 and WS_2-$MoSe_2$-WSe_2), and superlattices (such as WS_2-WSe_2-WS_2-WSe_2-WS_2) were readily prepared with precisely controlled spatial modulation. Transmission electron microscope studies showed clear chemical modulation with atomically sharp interfaces. Electrical transport studies of WSe_2-WS_2 lateral junctions showed well-defined diode characteristics with a rectification ratio up to 10^5.

The two-dimensional (2D) atomic crystals of transition-metal dichalcogenides (TMDs) (e.g., MoS_2, $MoSe_2$, WS_2, and WSe_2) have attracted intense recent interest (*1*–*11*). To explore the full potential of these 2D atomic crystals requires reliable synthesis of their heterostructures and superlattices with precisely defined spatial modulation of chemical compositions and electronic structures. Despite considerable efforts and some successful examples to date (*12*–*21*), robust synthesis of the atomically thin 2D TMD heterostructures remains a substantial challenge, and epitaxial growth of 2D superlattices with multiple alternating blocks has not been realized.

To date, diverse monolayer atomic crystals, as well as their alloys, have been successfully grown via chemical vapor deposition (CVD) or thermal CVD process by using various chemical vapor sources (*22*–*33*). With a similar crystal structure and comparable lattice constants among these 2D crystals, in-domain lateral heterostructures have also been successfully synthesized through a two-step epitaxial growth of a second material (e.g., $MoSe_2$, WSe_2) at the edge of an existing domain of a first material (e.g., MoS_2, WS_2) (*12*–*21*). In principle, such sequential growth process can be repeated multiple times for the block-by-block growth of multiheterostructures (with multiple distinct material blocks) or superlattices (with multiple alternating blocks) by switching the chemical vapor source or modulating the exact growth conditions in each growth step.

To rationally produce lateral heterostructures with multiple distinct material blocks requires sequential growth steps with different chemical supply, growth conditions, or both. The monolayer 2D crystals are usually too delicate to survive multiple sequential growth steps necessary for the formation of 2D heterostructures or superlattices. With just a single or a few atomic layers, the 2D crystals essentially have little tolerance for any thermal-induced degradation and are more challenging to grow than other bulk or nanoscale heterostructures with more atomic layers. Additionally, the ill-controlled supply of chemical vapor sources during the temperature swing stage between the sequential growth steps often leads to undesired homogeneous nucleation. To experimentally realize robust step-by-step growth of atomically thin 2D heterostructures or superlattices, at least two key requirements must be satisfied. First, the nucleating block must be robust enough to survive the temperature or chemical environment swing between sequential growth steps. Second, undesired homogeneous nucleation of the new crystal seeds must be minimized and ensure exclusive heterogeneous epitaxial growth at the edge of the existing 2D crystals.

Although the growth of 2D heterostructures has been demonstrated, studies to date are largely

[1]State Key Laboratory for Chemo/Biosensing and Chemometrics, College of Chemistry and Chemical Engineering, Hunan University, Changsha 410082, China. [2]Center for Electron Microscopy, Institute for New Energy Materials and Low-Carbon Technologies, School of Materials, Tianjin University of Technology, Tianjin 300384, China. [3]Department of Chemistry and Biochemistry and California Nanosystems Institute, University of California, Los Angeles, CA 90095, USA.
*These authors contributed equally to this work. †Corresponding author. Email: xidongduan@hnu.edu.cn; xduan@chem.ucla.edu

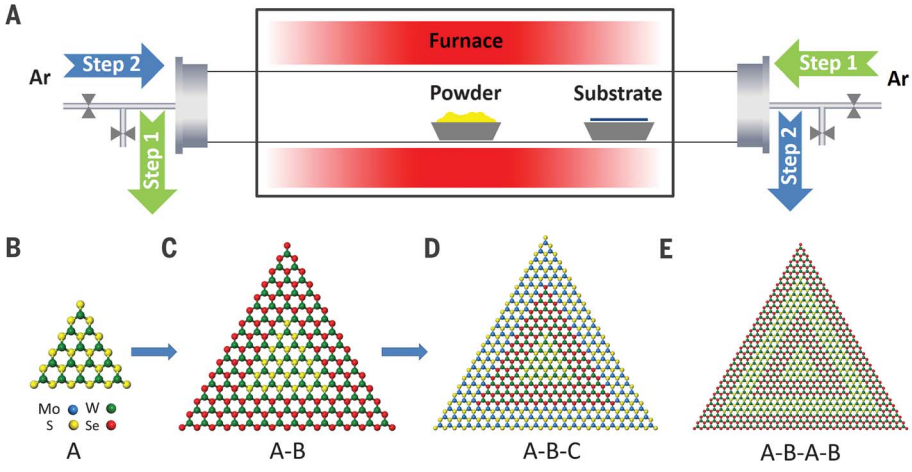

Fig. 1. Robust epitaxial growth of 2D monolayer heterostructures, multiheterostructures, and superlattices with a modified CVD process. (**A**) Schematic illustration of a modified CVD system for the robust epitaxial growth of lateral heterostructures. The solid powders were directly used as the source material. Both sides of the quartz tube are equipped with a gas inlet and outlet. The direction of argon gas flow can be switched by using the angle-style valves at the two ends of the quartz tube. A reverse flow from the substrate to the source is applied during the temperature ramping and stabilization stage to cool existing 2D crystals on the substrate and prevent unintended supply of vapor source reactant or uncontrolled nucleation and growth (step 1). After reaching the desired growth temperature, a forward flow from the source to the substrate is applied to transport the vapor phase reactant onto the growth substrate for the epitaxial growth of the desired 2D crystals (step 2). The reverse flow can effectively prevent the unintended homogeneous nucleation and minimize thermal degradation of the atomically thin 2D crystals to ensure highly robust sequential growth of (**B**) monolayer seed A, (**C**) A-B heterostructure, (**D**) A-B-C multiheterostructure, and (**E**) A-B-A-B superlattice.

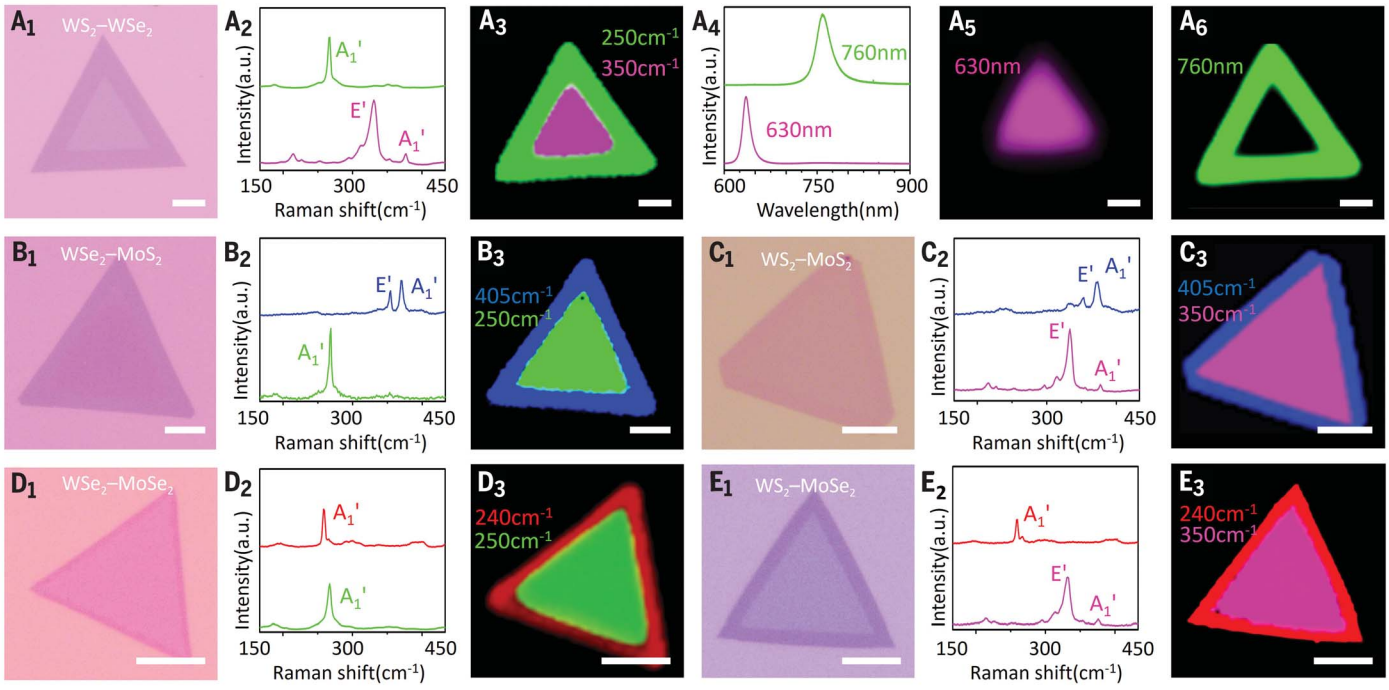

Fig. 2. General growth of diverse 2D lateral heterostructures. (**A$_1$**) Optical microscope image of a WS_2-WSe_2 heterostructure domain. (**A$_2$**) Raman spectra of the WS_2-WSe_2 heterostructure. The pink curve is obtained from the center region, showing the characteristic Raman peaks of WS_2, and the green curve is obtained from the peripheral region, showing the characteristic Raman peaks of WSe_2. (**A$_3$**) Spatially resolved Raman mapping image shows clear lateral integration of the WS_2-WSe_2 heterostructure. (**A$_4$**) Photoluminescence (PL) spectra of the WS_2-WSe_2 heterostructure. The pink curve is obtained from the center region, showing the characteristic PL peak of WS_2, and the green curve is obtained from the peripheral region, showing the characteristic PL peak of WSe_2. (**A$_5$** and **A$_6$**) Spatially resolved PL mapping images at 630 and 760 nm, showing characteristic PL emission of WS_2 and WSe_2 in the center and peripheral regions of the triangular domain. (**B$_1$** to **B$_3$**) Optical microscope image, Raman spectra, and mapping image of monolayer WSe_2-MoS_2 heterostructure. (**C$_1$** to **C$_3$**) Optical microscope image, Raman mapping spectra, and image of monolayer WS_2-MoS_2 heterostructure. (**D$_1$** to **D$_3$**) Optical microscope image, Raman spectra, and mapping image of monolayer WSe_2-$MoSe_2$ heterostructure. (**E$_1$** to **E$_3$**) Optical microscope image, Raman spectra, and mapping image of monolayer WS_2-$MoSe_2$ heterostructure. All scale bars are 5 μm.

limited to the simplest heterostructures with only two distinct material blocks for a few selected material combinations. The growth of multi-heterostructures or superlattices with three or more distinct material blocks, which requires sequential growth with multiple back-and-forth swings between the less and more aggressive synthetic conditions, makes it inevitable that existing blocks will be damaged when the subsequent growth step is carried out in a more aggressive condition (e.g., higher temperature) than the prior step.

We designed a modified step-by-step thermal CVD process in which a selected source powder is heated and vaporized under a flow of argon carrier gas for each sequential step, and the heterostructures are formed by the continued lateral epitaxial growth at the edge of the first monolayer crystals placed at the downstream end of the CVD furnace [further details of the modified growth process are in the supplementary materials (*34*)]. In a typical sequential-growth process, the excessive thermal degradation (fig. S1) or uncontrolled nucleation (fig. S2) during the temperature swing between sequential growth steps represents the key obstacle to reliable formation of monolayer heterostructures. To avoid such adverse effects, we used a reverse flow from the substrate to the source during the temperature swing between successive growth steps (Fig. 1A). A forward flow from the chemical vapor source was only applied at the exact growth temperature. With such reverse flow, the existing monolayer materials on the growth substrate were continuously flushed by the cold argon gas during the temperature swing to reduce exposure to high temperature and minimize thermal degradation. The reverse flow from the substrate to the source during the temperature ramping-up stage could also prevent unintended supply of the chemical vapor source at undesired temperature to eliminate uncontrolled homogeneous nucleation. With a high degree of controllability in each step, the integrity and quality of monolayer heterostructures can be well preserved after multiple sequential growth steps. This approach can thus offer a general and reliable strategy for the growth of a wide range of heterostructures, multiheterostructures, and superlattices (Fig. 1, B to E, and fig. S3).

We used our approach initially for the general synthesis of a wide range of 2D crystal heterostructures. Figure 2A$_1$ shows the optical microscope image of a synthesized triangular domain of WS_2-WSe_2 monolayer heterostructure on a SiO_2/Si substrate, which exhibits two concentric regions with slightly different optical contrast. Atomic force microscope (AFM) studies show that the heterostructure domain exhibits a smooth surface with a single step-height of 0.75 nm (fig. S4), confirming the monolayer nature of the heterostructure domain. To probe the spatial modulation of the structural and optical properties in the resulting WS_2-WSe_2 heterostructures, we conducted micro-Raman and micro-photoluminescence (micro-PL) studies using a confocal Raman microscope. The Raman spectra taken from the center and peripheral regions of the triangular domain clearly show distinct features. The Raman spectrum from the center region exhibits two prominent peaks at 350 and 419 cm^{-1} (pink line in Fig. 2A$_2$), corresponding to the E′ and A$_1$′ resonance modes of WS_2, whereas the Raman spectrum from the peripheral region displays one prominent peak at 250 cm^{-1} (green line in Fig. 2A$_2$), in agreement with the A$_1$′ resonance modes of WSe_2 (*35*, *36*). These micro-Raman studies demonstrate the coexistence of two distinct materials within the same triangular domain. The spatially resolved Raman mapping studies further reveals the spatial modulation within the triangular domain, with the center part consisting of a triangular domain of WS_2 and the peripheral region composed of WSe_2 (Fig. 2A$_3$).

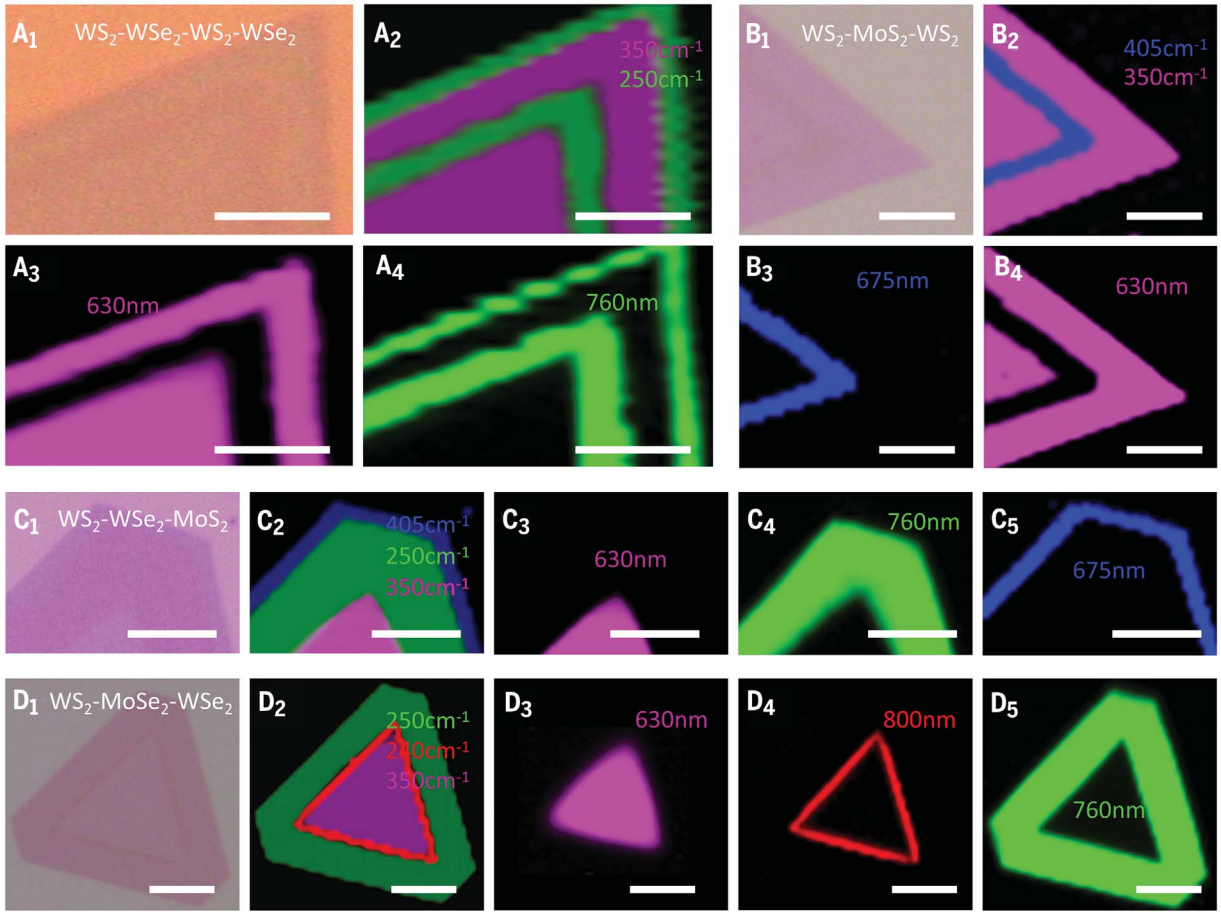

Fig. 3. Raman and photoluminescence characterizations of 2D superlattices and multiheterostructures. (**A_1**) Optical microscope image of WS_2-WSe_2-WS_2-WSe_2 superlattice on SiO_2/Si substrate. (**A_2**) Raman mapping image at 250 and 350 cm^{-1} clearly shows the WS_2-WSe_2 superlattice structure. (**A_3** and **A_4**) PL mapping images at 630 and 760 nm further confirm the WS_2-WSe_2 lateral superlattice structure. (**B_1** to **B_4**) Optical microscope image, Raman mapping, and PL mapping images of the WS_2-MoS_2-WS_2 multiheterostructure on SiO_2/Si. Raman mapping at 405 and 350 cm^{-1} clearly shows the formation of WS_2-MoS_2-WS_2 multiheterostructure, which is confirmed by PL mapping images at 675 and 630 nm. (**C_1** to **C_5**) Optical microscope image, Raman mapping, and PL mapping of the WS_2-WSe_2-MoS_2 multiheterostructure on SiO_2/Si. Raman mapping at 405, 250, and 350 cm^{-1} clearly shows the formation of WS_2-WSe_2-MoS_2 multiheterostructure, which is confirmed by PL mapping images at 630, 760, and 675 nm. (**D_1** to **D_5**) Optical microscope image, Raman mapping, and PL mapping of the WS_2-$MoSe_2$-WSe_2 multiheterostructure on SiO_2/Si. Raman mapping at 250, 240, and 350 cm^{-1} clearly shows the formation of WS_2-$MoSe_2$-WSe_2 multiheterostructure, which is confirmed by PL mapping images at 630, 800, and 760 nm. All scale bars correspond to 5 μm.

Similarly, micro-PL studies also show highly distinct photoluminescence peaks at 630 nm for the center part and 760 nm for the peripheral part (Fig. 2A_4), consistent with the near band-edge emission from monolayer WS_2 and WSe_2, respectively (*36*, *37*). The PL mapping studies (Fig. 2, A_5 and A_6) show features similar to those of Raman mapping studies, further confirming the formation of WS_2-WSe_2 lateral heterostructures. The PL spectra at the interface region display two distinct peaks (fig. S5A), with the peak positions displaying little deviation from those of the center region (WS_2) or the peripheral region (WSe_2). The simple overlap of the PL spectra at the interface indicates a rather sharp transition from WS_2 to WSe_2 at the interface of the synthesized lateral heterostructure (*13*), as will be further demonstrated below. Using the same strategy, we synthesized a wide range of monolayer heterostructures including WSe_2-MoS_2 (Fig. 2, B_1 to B_3), WS_2-MoS_2 (Fig. 2, C_1 to C_3), WSe_2-$MoSe_2$ (Fig. 2, D_1 to D_3), and WS_2-$MoSe_2$ (Fig. 2, E_1 to E_3), which, as shown by optical microscopy, Raman spectroscopy, and PL mapping studies (fig. S6), formed lateral heterojunctions similar to the WS_2-WSe_2 heterostructures.

We also grew more complex compositionally modulated superlattices or multiheterostructures through a step-by-step growth process, in which the number of periods and repeated spacing can be readily varied during growth. The optical microscope image of a synthesized WS_2-WSe_2-WS_2-WSe_2 monolayer superlattice on a SiO_2/Si substrate (Fig. 3A_1) exhibited four concentric regions with slightly different optical contrast. The spatially resolved Raman mapping at 350 cm^{-1} (E′ mode of WS_2) and 250 cm^{-1} (A_1′ mode of WSe_2) (Fig. 3A_2) revealed the spatial modulation of the triangular domain, with the first and third parts composed of WS_2 and the second and fourth parts composed of WSe_2. Thus, a seamless lateral superlattice structure formed within the same triangular domain. The PL mapping images at 630 nm (near band-edge emission of WS_2; Fig. 3A_3) and 760 nm (near band-edge emission of WSe_2; Fig. 3A_4) also confirmed the formation of a WS_2-WSe_2 monolayer lateral superlattice structure. In addition to the lateral superlattices, monolayer lateral multiheterostructures including WS_2-MoS_2-WS_2, WS_2-WSe_2-MoS_2, and WS_2-$MoSe_2$-WSe_2 were synthesized, and optical microscopy, Raman, and PL characterizations of these lateral multiheterostructures confirmed the formation of multiheterostructures with well-defined spatial modulation (Fig. 3, B_1 to D_5).

The detailed atomic structure of the lateral heterostructure interface was revealed by high-angle

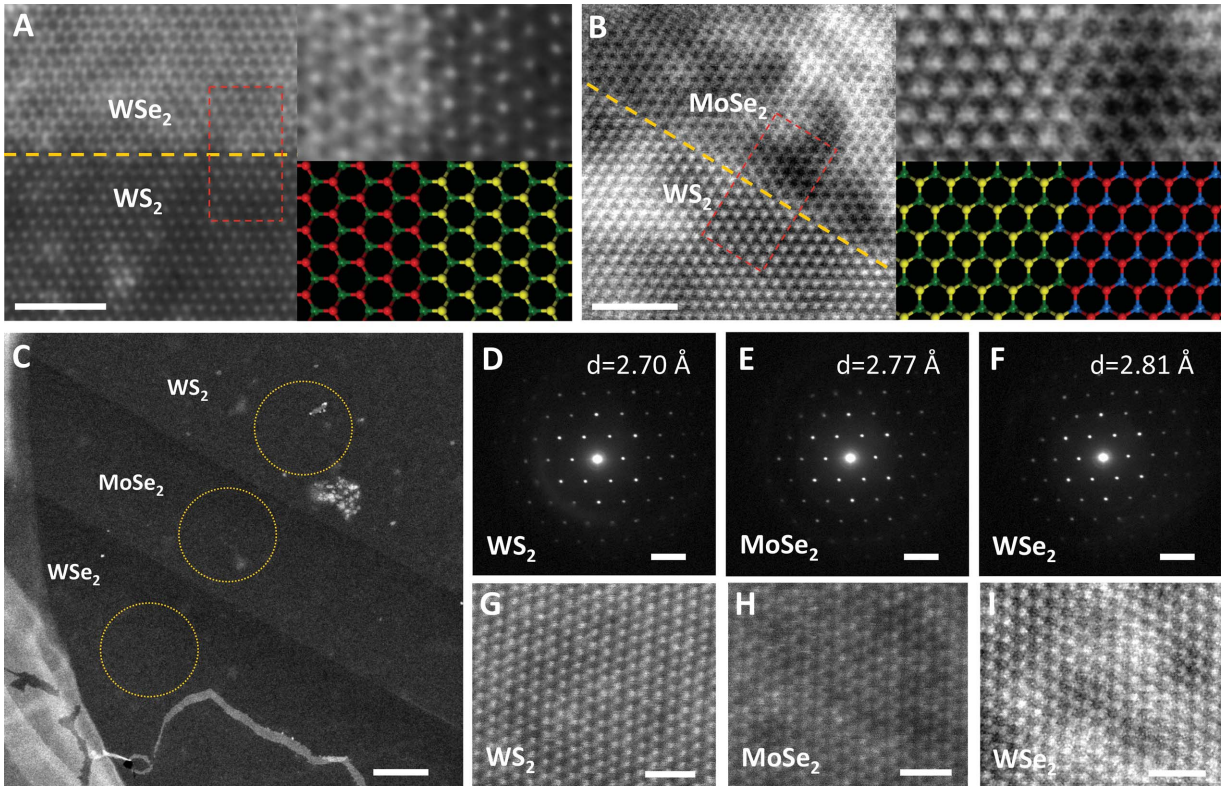

Fig. 4. Atomic structure of the lateral heterostructures and multiheterostructures. (**A**) Atomic-resolution *Z*-contrast STEM image taken from the WS_2-WSe_2 lateral heterostructure (left). Magnified STEM image of the dashed red rectangle region (top right) and the corresponding atomic model (bottom right). The orange dashed lines highlight the atomically sharp interface (interline). Scale bar, 2 nm. (**B**) Atomic-resolution *Z*-contrast STEM image taken from the WS_2-$MoSe_2$ lateral heterostructure (left). Magnified STEM image of the dashed red rectangle region (top right) and the corresponding atomic model (bottom right). The orange dashed lines highlight the atomically sharp interline. Scale bar, 2 nm. (**C**) Low-magnification *Z*-contrast image of the lateral WS_2-$MoSe_2$-WSe_2 multiheterostructure. Scale bar, 100 nm. (**D** to **F**) Electron diffraction patterns taken from the yellow dotted circle regions in (C), corresponding to the WS_2 region (D), $MoSe_2$ region (E), and WSe_2 region (F). Scale bar, 5 nm^{-1}. (**G** to **I**) Atomic-resolution STEM image taken from the WS_2 region (G), $MoSe_2$ region (H), and WSe_2 region (I). Scale bar, 1 nm.

annular dark-field scanning transmission electron microscope (HAADF-STEM) *Z*-contrast imaging. Figure 4A shows a *Z*-contrast image of the WS_2-WSe_2 lateral interface, where Se atoms exhibit higher image intensity than the S atoms. The atomically sharp interface can be clearly observed along the overall straight "interline" in the WS_2-WSe_2 lateral junction. The WS_2 and WSe_2 domains connect seamlessly at the interface into a single hexagonal monolayer lattice and share the same crystal orientation. The corresponding atomic model, obtained via atom-by-atom image quantification, indicates the seamless connection and atomically abrupt transition between the WS_2 and WSe_2 lattice. Figure 4B further shows the atomic structure of WS_2-$MoSe_2$ lateral junction, where an atomically sharp interline was also well resolved.

We further investigated the structural modulation across the WS_2-$MoSe_2$-WSe_2 multiheterostructure using the low-magnification *Z*-contrast image. Three regions with slightly different contrasts were observed, corresponding to WS_2, $MoSe_2$, and WSe_2, respectively. The selected area electron diffraction (SAED) patterns were taken at the WS_2 region, $MoSe_2$ region, and WSe_2 region, respectively (Fig. 4, D to F). The hexagonally arranged diffraction spots can be indexed to the hexagonal symmetry of the [001] zone plane of WS_2, $MoSe_2$, and WSe_2 lattice structures. A careful analysis of these diffraction peaks yields (100) lattice plane spacings of 2.70, 2.77, and 2.81 Å, in agreement with the values for WS_2, $MoSe_2$, and WSe_2, respectively (*12*, *38*). Figure 4, G to I, show the high-resolution STEM images of WS_2, $MoSe_2$, and WSe_2. On the basis of these images, we could also determine the (100) lattice plane spacings of WS_2, $MoSe_2$, and WSe_2 to be 2.70, 2.79, and 2.81 Å, respectively, consistent with the lattice plane spacings yielded from the SAED studies. Together, these studies demonstrate the well-defined chemical and structural modulation in 2D crystal heterostructures and multiheterostructures with atomically sharp interfaces.

With the atomically sharp interface, the width of heteroepitaxy can be controlled down to the nanometer scale (fig. S7), which may enable the realization of ultrashort-period superlattices or open a path to multi–quantum-well (or "quantum-line") structure in the 2D atomic crystals. To further characterize the electronic properties of the monolayer heterostructures, we also fabricated a monolayer lateral p-n junction device from WSe_2-WS_2 lateral heterostructures by taking advantage of the intrinsically p-type characteristics of WSe_2 and the n-type characteristics of WS_2. The current-versus-voltage measurements showed a rectification ratio up to 10^5 (fig. S8), consistent with the presence of a monolayer lateral p-n junction. The robust synthesis of diverse 2D heterostructures and superlattices with atomically sharp interfaces creates an interesting material system for fundamental studies and novel device demonstrations at the limit of single-atom thickness, which will be an important topic for future studies. Furthermore, by using site-specific nucleating blocks obtained from lithography patterning or patterned growth (*39*), a similar sequential epitaxial growth may be used for producing complex heterostructures with controlled location and orientation, which will be important for developing practical technologies from these atomically thin crystals.

REFERENCES AND NOTES

1. K. S. Novoselov *et al.*, *Proc. Natl. Acad. Sci. U.S.A.* **102**, 10451–10453 (2005).

2. Q. H. Wang, K. Kalantar-Zadeh, A. Kis, J. N. Coleman, M. S. Strano, *Nat. Nanotechnol.* **7**, 699–712 (2012).
3. A. M. Jones *et al.*, *Nat. Phys.* **10**, 130–134 (2014).
4. A. Pospischil, M. M. Furchi, T. Mueller, *Nat. Nanotechnol.* **9**, 257–261 (2014).
5. C.-H. Lee *et al.*, *Nat. Nanotechnol.* **9**, 676–681 (2014).
6. W. J. Yu *et al.*, *Nat. Mater.* **12**, 246–252 (2013).
7. B. W. H. Baugher, H. O. H. Churchill, Y. Yang, P. Jarillo-Herrero, *Nat. Nanotechnol.* **9**, 262–267 (2014).
8. W. J. Yu *et al.*, *Nat. Nanotechnol.* **8**, 952–958 (2013).
9. P. Rivera *et al.*, *Science* **351**, 688–691 (2016).
10. S. Wu *et al.*, *Nature* **520**, 69–72 (2015).
11. S. B. Desai *et al.*, *Science* **354**, 99–102 (2016).
12. X. Duan *et al.*, *Nat. Nanotechnol.* **9**, 1024–1030 (2014).
13. M.-Y. Li *et al.*, *Science* **349**, 524–528 (2015).
14. Y. Gong *et al.*, *Nat. Mater.* **13**, 1135–1142 (2014).
15. C. Huang *et al.*, *Nat. Mater.* **13**, 1096–1101 (2014).
16. Y. Yoo, Z. P. Degregorio, J. E. Johns, *J. Am. Chem. Soc.* **137**, 14281–14287 (2015).
17. M. Mahjouri-Samani *et al.*, *Nat. Commun.* **6**, 7749 (2015).
18. C. Tan, H. Zhang, *J. Am. Chem. Soc.* **137**, 12162–12174 (2015).
19. K. Chen *et al.*, *ACS Nano* **9**, 9868–9876 (2015).
20. X.-Q. Zhang, C.-H. Lin, Y.-W. Tseng, K.-H. Huang, Y.-H. Lee, *Nano Lett.* **15**, 410–415 (2015).
21. J. Chen *et al.*, *Chem. Mater.* **28**, 7194–7197 (2016).
22. K.-K. Liu *et al.*, *Nano Lett.* **12**, 1538–1544 (2012).
23. Y.-H. Lee *et al.*, *Adv. Mater.* **24**, 2320–2325 (2012).
24. K. Kang *et al.*, *Nature* **520**, 656–660 (2015).
25. Y.-H. Lee *et al.*, *Nano Lett.* **13**, 1852–1857 (2013).
26. A. M. van der Zande *et al.*, *Nat. Mater.* **12**, 554–561 (2013).
27. M. Zhao *et al.*, *Nat. Nanotechnol.* **11**, 954–959 (2016).
28. Y. Zhang *et al.*, *ACS Nano* **7**, 8963–8971 (2013).
29. X. Wang *et al.*, *ACS Nano* **8**, 5125–5131 (2014).
30. J. Mann *et al.*, *Adv. Mater.* **26**, 1399–1404 (2014).
31. X. Lu *et al.*, *Nano Lett.* **14**, 2419–2425 (2014).
32. H. Li *et al.*, *J. Am. Chem. Soc.* **136**, 3756–3759 (2014).
33. S. Tongay *et al.*, *Appl. Phys. Lett.* **104**, 012101 (2014).
34. See the supplementary materials.
35. W. Zhao *et al.*, *Nanoscale* **5**, 9677–9683 (2013).
36. H. R. Gutiérrez *et al.*, *Nano Lett.* **13**, 3447–3454 (2013).
37. H. Sahin *et al.*, *Phys. Rev. B Condens. Matter* **87**, 165409 (2013).
38. R. Coehoorn *et al.*, *Phys. Rev. B* **35**, 6195–6202 (1987).
39. Y. Zhou *et al.*, *ACS Nano* **8**, 1485–1490 (2014).

ACKNOWLEDGMENTS

We acknowledge support from the National Natural Science Foundation of China (no. 61528403). J.L. acknowledges support from the National Program for Thousand Young Talents of China, Tianjin Municipal Science and Technology Commission (15JCYBJC52600), and Tianjin Municipal Education Commission. X.F.D. acknowledges support from the National Science Foundation DMR1508144. All data are reported in the main text and supplementary materials.

SUPPLEMENTARY MATERIALS

www.sciencemag.org/content/357/6353/788/suppl/DC1
Materials and Methods
Supplementary Text
Figs. S1 to S8
Table S1

18 May 2017; accepted 19 July 2017
Published online 3 August 2017
10.1126/science.aan6814

Science

Robust epitaxial growth of two-dimensional heterostructures, multiheterostructures, and superlattices

Zhengwei Zhang, Peng Chen, Xidong Duan, Ketao Zang, Jun Luo and Xiangfeng Duan

Science **357** (6353), 788-792.
DOI: 10.1126/science.aan6814originally published online August 3, 2017

Cycling 2D crystal growth

The electronic and optical properties of two-dimensional (2D) transitional metal dichalcogenides such as MoS_2 and WSe_2 could be modulated by creating in-plane superlattices and heterostructures from these materials. However, single layers of these materials are fragile and often do not withstand the processing conditions needed during subsequent growth steps. Zhang *et al.* developed a reverse-flow reactor that avoids thermal degradation and unwanted crystal nucleation. They demonstrate several examples of block-by-block epitaxial growth, such as 2D heterostructures where MoS_2 surrounds a WS_2 core and superlattices where the composition alternates between WS_2 and WSe_2.

Science, this issue p. 788